Embryonic tissues as active foams

Sangwoo Kim [1], Marie Pochitaloff[1], Georgina A. Stooke-Vaughan[1] and Otger Campàs [1,2,3,4,5] ✉

The physical state of embryonic tissues emerges from non-equilibrium, collective interactions among constituent cells. Cellular jamming, rigidity transitions and characteristics of glassy dynamics have all been observed in multicellular systems, but it is unclear how cells control these emergent tissue states and transitions, including tissue fluidization. Combining computational and experimental methods, here we show that tissue fluidization in posterior zebrafish tissues is controlled by the stochastic dynamics of tensions at cell–cell contacts. We develop a computational framework that connects cell behaviour to embryonic tissue dynamics, accounting for the presence of extracellular spaces, complex cell shapes and cortical tension dynamics. We predict that tissues are maximally rigid at the structural transition between confluent and non-confluent states, with actively generated tension fluctuations controlling stress relaxation and tissue fluidization. By directly measuring strain and stress relaxation, as well as the dynamics of cell rearrangements, in elongating posterior zebrafish tissues, we show that tension fluctuations drive active cell rearrangements that fluidize the tissue. These results highlight a key role of non-equilibrium tension dynamics in developmental processes.

Many essential processes in multicellular organisms, from organ formation to tissue homoeostasis, require a tight control of the tissue physical state[1,2]. While tissue mechanics and structure at supracellular scales emerge from the collective physical interactions among the constituent cells, their control occurs at cell and subcellular levels. Bridging these scales is essential to understand the physical nature of active multicellular systems and to identify the processes that cells use to control the physical state of embryonic tissues.

In vitro experiments of cell monolayers on synthetic substrates have revealed characteristics of glassy dynamics[3,4] and rigidity transitions[5–7], which are thought to be linked to biological function and multiple pathologies. In contrast, suspended epithelial monolayers are largely solid-like in vitro[8] and show evidence of fracture in vivo[9]. Experiments with embryonic tissues have shown characteristics of glassy dynamics in cell movements[10], viscous behaviour at long timescales[11] and also structural signatures reminiscent of jamming transitions[12], with cell divisions, cell shape and/or changes in cell adhesion suspected to play a role in the control of these emergent behaviours[5,11,13,14]. Recent in vivo experiments in developing zebrafish embryos showed the existence of a rigidity transition underlying the formation of the vertebrate body axis, revealing a functional role of rigidity transitions in embryonic development[15] (Fig. 1a). Both the presence of adhesion-dependent spaces between cells (Fig. 1b–d) and the dynamics of cell–cell contacts (Fig. 1e,f) were shown to influence the physical state of the tissue[15]. However, the relative roles of cell adhesion and cell–cell contact dynamics in the control of posterior tissue fluidization are still unclear. In general, little is known about how different cell behaviours control rigidity transitions and tissue fluidization in embryonic tissues, and whether all these observed emergent phenomena share a common physical origin.

The physical behaviour of multicellular systems has been studied theoretically using various approaches. Vertex models[16–21] and cellular Potts models[22,23] account for cell geometry and use equilibrium formulations to describe the physical state of the system. These descriptions predict a density-independent rigidity transition in confluent systems that depends on the balance between actomyosin-generated cortical tension T_0 and cell adhesion W (treated as passive, effective tensions), with the resulting cell shape being the control parameter for solid/fluid states[17]. Since cell shape plays a central role in models of confluent systems, the ability to accurately describe complex cell shapes, beyond polygonal shapes, may be important to understand the physical state of the system, as recently suggested[24,25]. Non-vertex models of deformable particles have instead focused on configurations in non-confluent equilibrium systems, both in the presence[26,27] and absence of cell adhesion[24,28]. In contrast, self-propelled particle and Voronoi models that focus on cell movements on synthetic substrates account for the dynamics of the system and predict rigidity transitions that depend on cell density and self-propulsion[29,30]. All these descriptions capture some important aspects of the problem, but each neglects a subset of key cell behaviours and/or restricts the allowed configurations. No current theoretical description accounts for all observed relevant cell behaviours in a common framework, hindering our understanding of how cells control the emergent physical state of the tissue.

Dynamic vertex model with extracellular spaces

To study the dynamics of embryonic tissues and their physical state, we generalize two-dimensional (2D) vertex models by accounting for (1) extracellular spaces (Fig. 1b,c,g and Methods), (2) the stochastic dynamics of active cortical tensions (Fig. 1e,f) and (3) complex cell shapes (Fig. 1a,g and Methods). Unlike previous vertex models, we do not assume the existence of a preferred cell perimeter, as experimental evidence for this constraint is lacking. Instead, since cells actively control adhesion, cortical tension and osmotic pressure[1,2], we derive a physical description reminiscent of foams but with active tension dynamics. Tissue dynamics and structure, as well as cell movements and their shapes, are all determined by the dynamics of vertices (Fig. 1g), which follow from force balance, namely

[1]Department of Mechanical Engineering, University of California, Santa Barbara, CA, USA. [2]Center for Bioengineering, University of California, Santa Barbara, CA, USA. [3]Department of Molecular, Cellular and Developmental Biology, University of California, Santa Barbara, CA, USA. [4]California NanoSystems Institute, University of California, Santa Barbara, CA, USA. [5]Cluster of Excellence Physics of Life, TU Dresden, Dresden, Germany. ✉e-mail: campas@ucsb.edu
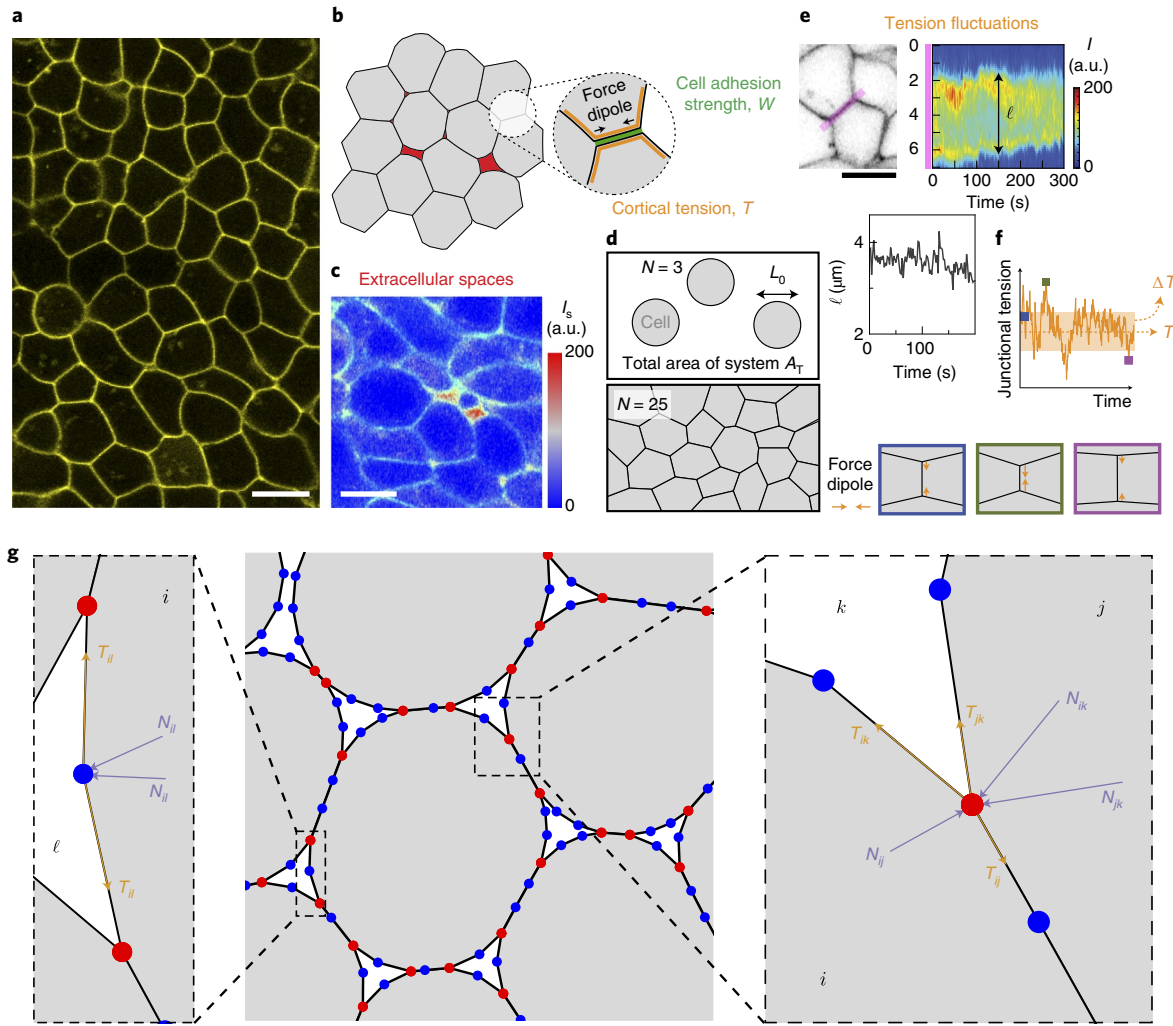
Fig. 1 | Characteristics of multicellular systems and simulation framework. a, Confocal section of embryonic tissue in a zebrafish embryo (membranes labelled, yellow). **b**, Schematics of cortical tension and adhesion at cell–cell contacts in a multicellular system with spaces (red) between cells (grey). **c**, Confocal section through zebrafish embryonic tissues showing the intensity (I_s) of fluorescent reporter protein secreted extracellularly as well as cell membranes (green), indicating the presence of extracellular spaces (red range). **d**, Schematics defining the cell size L_0, cell number N and simulation box area A_T, which specify cell density. **e**, Top: kymograph of membrane signal intensity (I) along a tissue region (pink, left) containing a cell–cell contact, showing contact length ℓ fluctuations (bottom). **f**, Top: simulated tension fluctuations causing cell–cell contact length fluctuations. Bottom: increasing (decreasing) tension shortens (lengthens) cell–cell junctions. **g**, Schematics of the dynamic vertex model formulation. Triple vertices (physical vertices, red) and non-physical intermediate vertices (blue) are shown. Scale bars, 10 μm.

$$\eta_R \frac{d\mathbf{R}_\alpha}{dt} = \sum_{i,j \in F(\alpha)} \left(\mathbf{T}_{ij} \, \Theta(T_{ij}) + \mathbf{N}_{ij} \right), \qquad (1)$$

where t is time, $\mathbf{R}_\alpha$ is the position of the vertex α, η_R is a friction coefficient characterizing the dissipation associated with moving a vertex, $\mathbf{T}_{ij}$ is the effective tension at the contact between cell i and j (with $F(\alpha)$ representing the set of all cells sharing vertex α) and $\mathbf{N}_{ij}$ is the normal forces acting on vertex α. $\Theta(\cdot)$ represents the Heaviside step function and prevents unrealistic negative tensions[15,31]. Normal forces arise from osmotic pressure differences in adjacent cells and are given by $N_{ij} = (\Delta P_i - \Delta P_j) L_{ij}/2$ (Methods), where L_{ij} and ΔP_i (ΔP_j) are, respectively, the contour length of the contact between cells i and j and the osmotic pressure difference across cell i (j).

To capture the observed fluctuating nature and finite persistence of tension dynamics[15], T_{ij}, we describe them as an Ornstein–Uhlenbeck process, with a tension that fluctuates around a fixed point T_{ij}^0 and has a persistence time τ_T (refs. [32,33]), specifically

$$\tau_T \frac{dT_{ij}}{dt} = -(T_{ij} - T_{ij}^0) + \Delta T \xi, \qquad (2)$$

where ΔT is the amplitude of tension fluctuations and ξ is Gaussian white noise (Fig. 1f and Methods). The fixed point effective tensions depend on both the average cortical tension, T_0, and average strength of cell–cell adhesion, W, which, like ΔT, are different at cell–cell contacts and free cell boundaries (Fig. 1b and Methods).

Scaling all quantities, we obtain the relevant dimensionless parameters (Table 1 and Methods). Since $P_0 L_0/T_0$ and τ_T/τ_R (Table 1) can be estimated from existing experimental data (Methods), we focus on the parameter space spanned by $\Delta T/T_0$, W/T_0 and the normalized cell density ρ (Table 1).

Structural transitions and mechanics of equilibrium systems

We first explore how the states and mechanics of the system change if spaces between cells are allowed. In the absence of tension

Table 1 | Definition of the relevant dimensionless parameters in the problem

| Dimensionless parameters	Description
$\Delta T/T_0$	Magnitude of tension fluctuations (Fig. 1e,f).
W/T_0	Relative strength of cell–cell adhesion W and average cortical tension T_0 (Fig. 1b).
$\rho \equiv NL_0^2/A_T$	Normalized system density (with A_T and N being the total area of the system and the number of cells, respectively; Fig. 1d).
P_0L_0/T_0	Relative magnitude of normal to tensional forces.
τ_T/τ_R	Ratio of persistence time of tension fluctuations and characteristic timescale $\tau_R \equiv \eta_T L_0/T_0$ of dissipation at vertices.

fluctuations ($\Delta T/T_0 = 0$), the amount of extracellular spaces in equilibrium configurations is determined by force balance and varies with both the cell density ρ and the relative cell adhesion strength W/T_0

(Fig. 2a). Increasing cell density results in larger cellular volume fraction ϕ (Fig. 2b) and cell contact number z (Fig. 2c), with the system eventually becoming confluent at an adhesion-dependent critical density, $\rho_c(W/T_0)$. For any fixed cell density, the system undergoes a non-confluent to confluent transition as W/T_0 is increased, since higher adhesion promotes stronger cell–cell contacts (Fig. 2a,b). These results extend previous studies for purely repulsive deformable particles[28] to arbitrary adhesion levels.

Changes in relative cell adhesion affect not only the volume fraction but also the structural characteristics of extracellular spaces. Equilibrium configurations sharply transition from a large number of small extracellular spaces to a few large extracellular spaces at $W/T_0 \approx 0.23$ (Fig. 2a,d), as small triangular extracellular spaces can only be stabilized below this value (Supplementary Section 1). Concomitant to the presence of large extracellular holes, which are reminiscent of epithelial fracture in vivo[9], the spontaneous clustering of cells strongly resembles flocculation in sticky emulsions[34,35] (Fig. 2a). Moreover, the system displays bistability between two possible equilibrium configurations for $W/T_0 \geq 0.23$, namely a confluent state with stretched cells and a non-confluent state with sparse and large extracellular holes (Fig. 2e), with strong hysteresis in
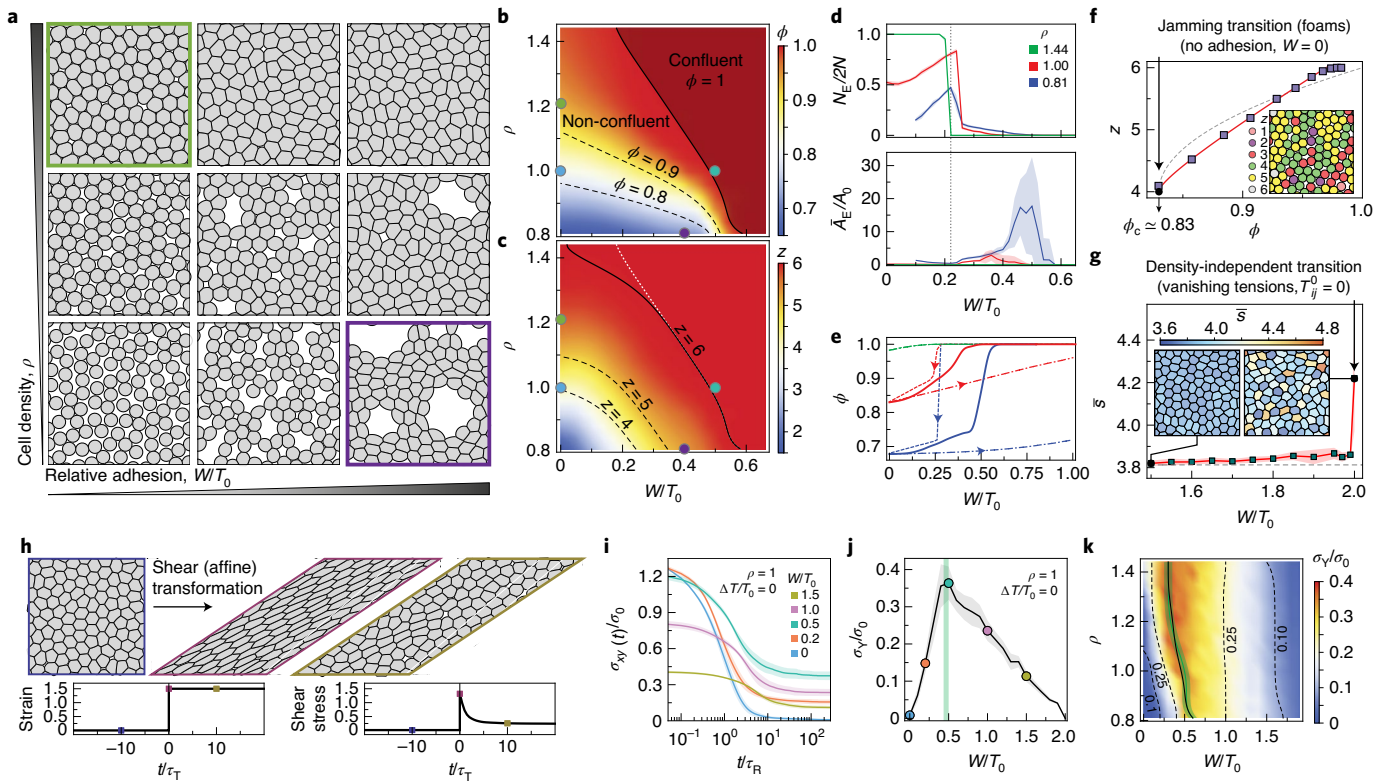
Fig. 2 | Equilibrium configurations and structural transitions. a–c, Representative equilibrium configurations (**a**), volume fraction ϕ (**b**) and mean number of neighbours z (**c**) for varying values of relative adhesion W/T_0 and cell density ρ. Green and purple boxes in **a** correspond to parameter values specified as circle dots of the same colour in **b** and **c**. **d,** Number N_E (top) and average area $\bar{A}_E$ (bottom) of extracellular spaces for varying relative cell adhesion and different cell densities, showing a sharp structural transition at $W/T_0 \approx 0.23$ (grey line) leading to the opening of large extracellular spaces. **e,** Lowering (dashed line) and increasing (dash-dotted line) relative adhesion quasistatically shows bistable states and strong hysteresis in equilibrium configurations. Equilibrium quenched states are also shown (solid line). **f,** Average neighbour number (cell contacts) z as the system volume fraction changes at vanishing cell adhesion, showing the existence of a jamming transition at $\phi_c \simeq 0.83$ and $z_c = 4$ (configuration shown in inset). Power-law fits $z - z_c = z_0(\phi - \phi_c)^{1/2} + z_1(\phi - \phi_c)$ with coefficients $z_0 \simeq 1.45$ and $z_1 \simeq 10.45$ (red line) and with $z_0 \simeq 4.85$ and $z_1 = 0$ (grey line) are shown. **g,** Average shape factor ($\bar{s}$) for varying relative adhesion showing a sharp increase at $W/T_0 = 2$ (vanishing tensions), leading to anisotropic cell shapes (inset), recapitulating density-independent transitions. **h,** Schematics of a simple shear deformation imposing a large strain step ($\epsilon_{xy} = 1.5$), with associated temporal evolution of both strain and shear stress. **i,** Temporal relaxation of shear stress σ_{xy} (normalized to $\sigma_0 \equiv \sqrt{\rho}\, T_0/L_0$) after the imposed strain step for varying adhesion levels. **j,k,** Dependence of the yield stress σ_Y on the relative adhesion strength (**j**) and on both cell density and relative adhesion (**k**), showing a maximum at the structural transition between confluent and non-confluent states (green line). Error bands, s.d.; $N = 20$ (**b–d,f,g**) and $N = 10$ (**e,i–k**) independent simulations for each parameter set.
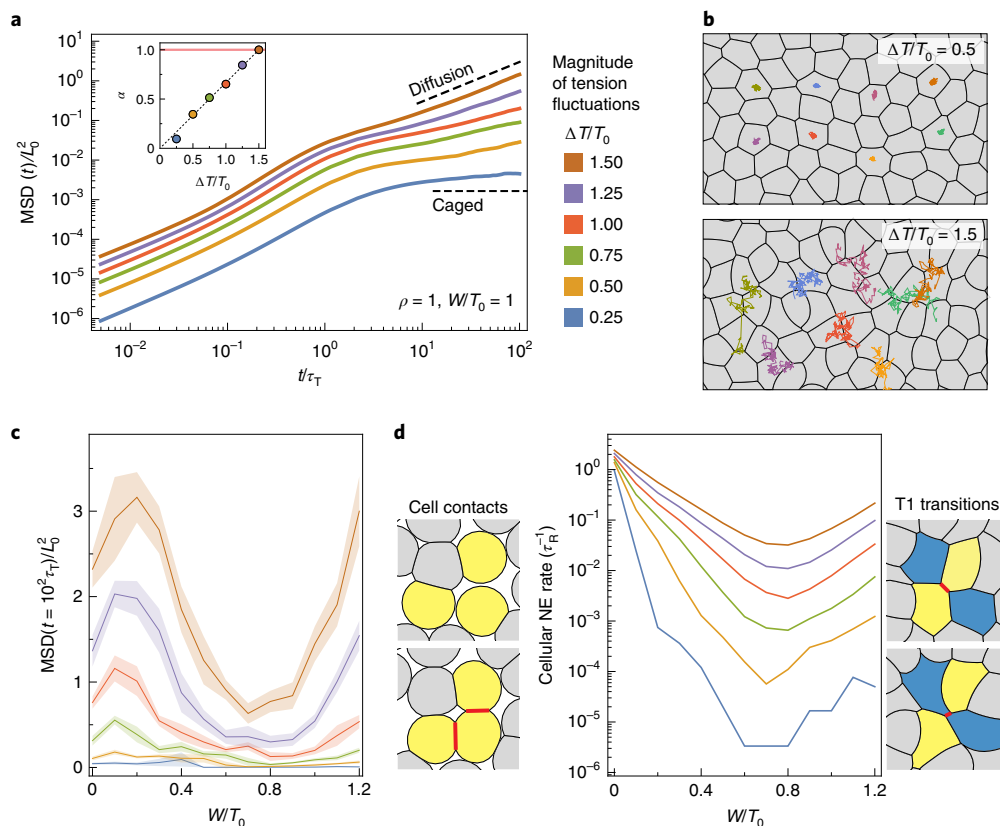
Fig. 3 | Tissue dynamics with finite tension fluctuations. a, MSD for varying magnitudes of tension fluctuations $\Delta T/T_0$, showing subdiffusive ($0 < \alpha < 1$) and diffusive ($\alpha = 1$) behaviours as tension fluctuations increase (inset). **b**, Snapshots of dynamic configurations with examples of cell trajectories over $t/\tau_T = 10^2$. **c**, MSD at long timescales ($t = 10^2 \tau_T \gg \tau_T > \tau_R$), showing non-monotonous behaviour for varying relative adhesion strength and minimal values at the structural transition. **d**, Cellular NE rate for varying relative adhesion. Distinct types of NE event: gain/loss of cell contacts (left) and T1 transitions (right). Cells and junctions undergoing NE events are highlighted as yellow/blue and red colour, respectively. Error bands, s.d.; $N = 10$ independent simulations for each set of parameters.

equilibrium configurations if adhesion or cortical tension are varied in a quasi-static manner (Fig. 2e, Supplementary Video 1 and Methods). Some of the predicted system configurations (Fig. 2a) are analogous to those previously obtained for equilibrium systems with open boundaries[27], but the bistability and hysteresis of configurations reported here can only be observed in closed systems that more closely resemble epithelial tissues.

In the limit of vanishing cell adhesion, the system should behave as foams/emulsions, which display a jamming transition at a critical value ϕ_c. The isostatic condition ($z_c = 4$ in 2D) sets the critical volume fraction $\phi_c \approx 0.83$ of the system[36] (Fig. 2f). Both this ϕ_c value and the power-law dependence of z (Fig. 2f) are in agreement with recent equilibrium simulations of deformable particles[28], indicating that our description accurately describes the foam limit. In the confluent limit, previous works reported density-independent rigidity transitions, which are controlled by the cell shape factor s ($s = P/\sqrt{A}$, with P and A being the cell perimeter and the area, respectively). The system switches from a solid to a fluid state at approximately $s_c \simeq 3.81$, with cells transiting from isotropic to anisotropic shapes[17,37,38]. The fluid state in these descriptions is characterized by vanishing effective tensions ($T_{ij}^0 = 0$), allowing neighbour exchanges (NEs) at no energetic cost[19]. Setting $W/T_0 = 2$ in our framework leads to vanishing effective tensions and a sharp increase in average shape factor due to the emergence of anisotropic cell shape (Fig. 2g), recapitulating density-independent transitions.

To directly assess the physical state of the system, we monitor shear-stress relaxation after imposing an affine deformation (Fig. 2h and Methods). The initial stress jump is largest with no adhesion and

vanishes when effective tensions vanish (Fig. 2i and Supplementary Fig. 5). Subsequently, shear stress relaxes with a characteristic timescale τ_R towards a constant value at long timescales, namely the yield stress σ_Y (ref. [39]), which depends non-monotonically on cell adhesion (Fig. 2j and Supplementary Video 2). For low relative adhesion W/T_0, the system is non-confluent and the yield stress increases with increasing adhesion as extracellular spaces close down. In contrast, for adhesion values leading to confluence, increasing W/T_0 leads to a decreasing yield stress due to lower effective tensions. Vanishing yield stress indicates a fluid tissue state, which occurs only for $W/T_0 = 0$ and $W/T_0 = 2$ and corresponds to the jamming transition (Fig. 2f) and the density-independent rigidity transition (Fig. 2g), respectively, with the tissue being solid for all other values in the $0 < W/T_0 < 2$ range. These results show that equilibrium systems are maximally rigid at the structural transition between confluent and non-confluent states (Fig. 2j,k), with increasing adhesion rendering the system more rigid in non-confluent systems and doing the opposite in confluent states.

Dynamics of active multicellular systems
Unlike equilibrium systems, tension dynamics at cell–cell contacts can drive cell movements, NEs and cell shape changes (Supplementary Videos 3 and 4). At timescales longer than all characteristic timescales ($t \gg \tau_T > \tau_R$), cell movements are caged for small $\Delta T/T_0$, as indicated by the saturation of the mean squared displacement (MSD) and bounded cell trajectories (Fig. 3a,b and Methods). For increasing magnitudes of tension fluctuations, cell uncaging starts to occur and the asymptotic behaviour of the MSD
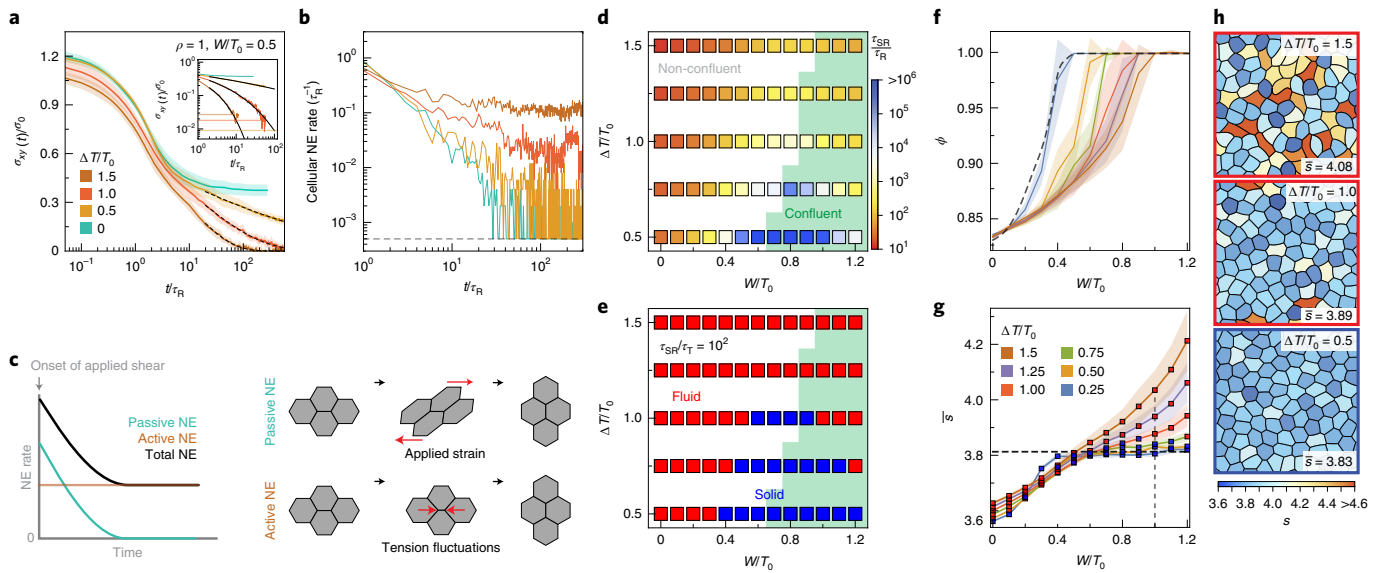
Fig. 4 | Stress relaxation and structure in active multicellular systems. a,b, Stress relaxation (**a**) and temporal changes in cellular NE rate (**b**) after the imposed strain step for varying magnitudes of tension fluctuations. The long timescale stress relaxation follows stretched exponentials (black dashed lines) and eventually reaches the average value σ_A of active shear-stress fluctuations (horizontal lines in inset). The cellular NE rate quickly decays to zero in the absence of activity ($t \approx \tau_R$), but remains finite in the presence of activity. **c**, Sketch showing the dynamics NE induced by the externally applied shear strain (passive) and by tension fluctuations in cells (active). Active NE enables further stress relaxation and tissue fluidization after the initial passively induced NE. **d**, Stress relaxation timescale τ_{SR} for varying magnitude of tension fluctuations and relative adhesion, showing a sharp increase as the structural transition between non-confluent and confluent (green background) states. **e**, Phase diagram showing the transition between fluid and solid tissue states for different activity values and relative adhesion strength. Solid states surround the structural transition and are found both in confluent and non-confluent configurations for low enough activity. **f–h**, Dependence of the system volume fraction ϕ (**f**) and average shape factor $\bar{s}$ (**g**; with red/blue squares indicating fluid/solid states, respectively) on relative adhesion for different magnitudes of tension fluctuations. Representative snapshots of dynamic configurations for fixed relative adhesion ($W/T_0 = 1$; vertical dashed line in **g**) and increasing tension fluctuations are shown **h**, with red and blue outlines indicating fluid and solid states, respectively. Error bands, s.d.; $N = 10$ independent simulations for each set of parameters.

for $t \gg \tau_T$ becomes a power law (MSD $\approx t^\alpha$), with an exponent α that increases with activity (Fig. 3a, inset). This evidences subdiffusive ($\alpha < 1$) cell movements for intermediate activities, and diffusive ($\alpha = 1$) behaviour for large enough tension fluctuations (Fig. 3a,b).

Comparing MSD values at long timescales ($t = 10^2 \tau_T \gg \tau_T > \tau_R$) shows that increasing tension fluctuations always leads to higher cell movements, regardless of cell adhesion strength, as recently reported for confluent systems[33]. However, for a fixed level of activity, MSD values vary non-monotonically as adhesion increases, displaying very reduced cell movements at the transition between non-confluent and confluent states (Fig. 3c). Similar to the MSD, the NE rate displays analogous non-monotonic behaviour, with minimal NE events at the structural transition. Close to confluence for high adhesion levels, the NE rate is dominated by T1 transitions and related to the MSD by MSD($t = 10^2 \tau_T$) $\approx k_{NE}^{3/4}$ (Extended Data Fig. 1), with the timescale for T1 transitions, $1/k_{NE}$, diverging as the activity vanishes, a signature of glassy dynamics. In contrast, at low adhesion levels leading to non-confluent states, loss and formation of new cell contacts dominate NE events (Fig. 3d) and the MSD and NE behaviours differ close to jamming. The non-monotonic behaviour of both MSD and NE events, with minimal values at the transition between non-confluent and confluent states, suggests that the non-equilibrium system is also maximally solid-like at the structural transition.

Physical state of active multicellular systems

To study the rigidity of active systems, we apply a shear-strain step and monitor stress relaxation, as described above (Fig. 2h). The presence of finite tension fluctuations qualitatively changes stress relaxation at long timescales compared with equilibrium systems,

displaying a slow stress decay rather than plateauing to a yield stress (Fig. 4a and Supplementary Video 5). This long timescale stress relaxation is driven by actively induced T1 transitions (Fig. 4b), and can be accurately described by a stretched-exponential function (Fig. 4a, inset), as previously done to explain the dynamics of systems with a large number of intrinsic timescales[40,41]. The stress relaxation timescale, τ_{SR}, at which shear stress reaches the level of active shear stress in the unperturbed system (Fig. 4a, inset, and Supplementary Fig. 2), varies by over five orders of magnitude as the magnitude of tension fluctuations or relative adhesion change slightly (Fig. 4d). While larger activity values reduce τ_{SR} monotonically, increasing the relative adhesion strength leads to non-monotonic changes in τ_{SR}, which rapidly increases in non-confluent states and displays the opposite behaviour in confluent states. The largest stress relaxation timescale occurs at the structural transition between non-confluent and confluent states, indicating that tissues are minimally fluid at long timescales close to this structural transition (Fig. 4d), consistent with the predicted low cell movements and NE rates close to the transition (Fig. 3c,d).

In contrast to previous equilibrium vertex models, our results show that a given tissue can behave as a fluid or a solid depending on the time necessary to form embryonic structures. If the characteristic timescale τ_d of developmental processes is larger (smaller) than the stress relaxation timescale τ_{SR}, namely $\tau_d/\tau_{SR} \gg 1$ ($\tau_d/\tau_{SR} \ll 1$), the tissue behaves as a fluid (solid). Using typical developmental timescales ($\tau_d \approx 1$–2 h; $\tau_d/\tau_T \approx 10^2$), we obtain the tissue phase diagram (Fig. 4e). Over a critical value of tension fluctuations, the tissue is always fluid regardless of cell adhesion levels. Below that critical activity value, the tissue is fluid at both low and high adhesion levels, but solid in between, in the region of the phase
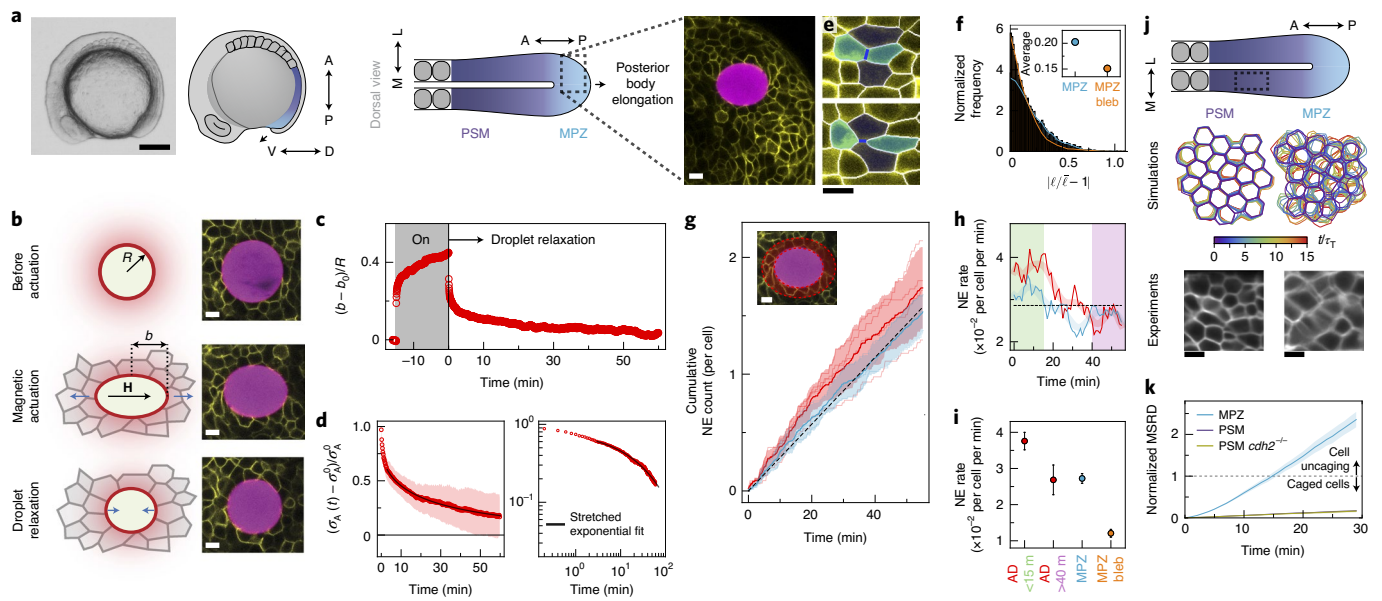
Fig. 5 | Stress relaxation and tissue fluidization in posterior tissues during body axis elongation. a, Lateral view of a zebrafish embryo (scale bar, 200 μm) and sketches showing lateral and dorsal views of posterior tissues, indicating the fluid-like MPZ and solid-like PSM (ventral, V; dorsal, D; anterior, A; posterior, P; medial, M; lateral, L). A confocal section showing a portion of the MPZ (cell membranes, yellow) with a magnetic droplet (magenta) is highlighted. **b**, Schematic sketches and confocal snapshots of magnetic droplet actuation in the MPZ tissue. **c**, Time evolution of the strain, $(b-b_0)/R$, before, during and after magnetic actuation. **d**, Relaxation of anisotropic stress $\sigma_A(t)$ after magnetic actuation in both linear and log-linear scales, with $\sigma_A^0 = \sigma_A(t=0)$. The fit (black line) corresponds to a stretched-exponential function. **e**, Example of NE events: cells in contact (blue line) before the T1 transition (cyan; top) and not in contact after the transition (bottom). **f**, Normalized frequency of amplitude of junctional length fluctuations for the MPZ, both in the absence and presence of blebbistatin (bleb; average amplitudes in inset). **g**, Cumulative NE events in the MPZ (away from the droplet, cyan; dashed black line shows linear fit) and in the close neighbourhood of the droplet (around droplet, red). Inset: visual definition of droplet neighbourhood (red). **h**, Temporal evolution of NE rate in the MPZ (cyan) and in the region around droplet (red). Initial ($t < 15$ min) and final ($t > 40$ min) stages of droplet relaxation are highlighted as green and pink shaded regions, respectively. **i**, Average NE rates in the region around droplet (AD, both during initial droplet relaxation (green) and at its final stages (pink)) and in the MPZ, both in the absence (cyan) and presence (orange) of blebbistatin. **j**, Experimentally measured and simulated dynamics of cell shapes in both the MPZ and the PSM, showing faster dynamics in the MPZ and largely static cell boundaries in the PSM. Experimental data are an average intensity projection of a confocal section timelapse. **k**, MSRD shows uncaging behaviour for the MPZ but caged for the PSM of both wild-type and $cdh2^{-/-}$ embryos. Error bands, s.d. (**d,g**) and s.e.m (**i,k**); $N = 10$ (**d**), $N = 298$ from 4 embryos (**g-i**, AD), $N = 396$ from 3 embryos (**g-i**, MPZ). Data in **f**, MPZ bleb in **i** and MSRD for MPZ and PSM in wild-type embryos in **k** were reanalysed from ref. [15]. Scale bars, 10 μm, unless otherwise stated.

diagram surrounding the structural transition between non-confluent and confluent states. This non-monotonic behaviour mirrors the behaviour of NE and cell movements, but care must be taken in inferring the physical state of the system solely from cellular movements (Extended Data Fig. 2). While cell density and cell shape are the control parameters associated with jamming transitions and density-independent transitions, respectively, our results show that tension fluctuations control a distinct rigidity transition in both confluent and non-confluent states, as suggested recently for confluent states[33].

To relate the mechanics of the system to its structure in the presence of tension dynamics, we study the configurations of the system. Tension fluctuations generally promote transitions from confluent to non-confluent states by opening up extracellular spaces at weak regions (Fig. 4f), implying that larger adhesion values are required to reach confluent states for increasing $\Delta T/T_0$. This effect becomes negligible for large cell densities ($\rho > 1$) and volume fraction is then solely determined by cell density ρ and relative cell adhesion W/T_0 (Supplementary Fig. 3). While cell shapes are only moderately affected by tension fluctuations in non-confluent regimes, with low shape factors associated with rounder cells, increasing tension fluctuations in confluent regimes leads to substantially larger shape factors (Fig. 4g,h). In contrast to density-independent transitions, where large shape factors (above approximately 3.81) result

from vanishing junctional tensions in fluid states[17], the large shape factors reported here are due to spatiotemporal tension fluctuations (Fig. 4h), with cell–cell contacts maintaining finite tensions (Supplementary Fig. 4 and Supplementary Video 6), as observed experimentally[31,42]. In particular, we find the presence of both fluid and solid tissue states for adhesion values in the range $0 < W/T_0 < 2$ that would correspond solely to solid states in previous equilibrium descriptions. These results indicate that the tissue fluid or solid state cannot be inferred from static measurements of cell shape factor only, as the tissue physical state and its structure depend strongly on the magnitude of tension fluctuations (Fig. 4g,h).

Fluidization of embryonic tissues

Our theoretical results indicate that in the presence of active tension fluctuations, active NE events control stress relaxation at long timescales both in confluent and non-confluent tissues. To experimentally address the role of tension fluctuations in stress relaxation and tissue fluidization, we employed magnetically responsive oil droplets to directly measure strain and stress relaxation in posterior tissues of developing zebrafish embryos (Fig. 5a), as these tissues have been previously shown to be in a fluid-like state[15]. After injecting a single droplet in the mesodermal progenitor zone (MPZ), we induced large droplet deformations of multiple cell diameters by applying a controlled magnetic field for a 15 min period[15,43]

(Fig. 5b,c and Methods). We subsequently monitored the droplet relaxation for 1 h after removing the magnetic field and measured the decay of stress in the tissue (Fig. 5d and Methods). We observed an initial fast decay (~30 s) followed by a very slow relaxation at long timescales that displays the stretched-exponential behaviour predicted theoretically for a fluctuation-induced stress relaxation (Fig. 4a). This slow relaxation was previously interpreted as a yield stress due to limitations in the measurement timescales[15], a well-known limitation in mechanical measurements of complex materials[39]. The present long timescale measurements reveal a very slow stress relaxation and indicate that posterior tissues completely fluidize on timescales of approximately 1 h, enabling nearly complete remodelling of posterior tissues during axis elongation, as this occurs at rates of approximately 45 μm h^{-1} (refs. [44,45]).

To address the role of active NE (T1 transitions) in tissue fluidization (Fig. 4c), we quantified the characteristics of NE events (Fig. 5e) during droplet relaxation in the MPZ, as cells in this region display considerable cell–cell contact fluctuations (Fig. 5f and Methods). Measurement of cumulative NE events in the MPZ (away from the droplet) shows a linear increase over time (Fig. 5g and Methods), indicating an approximately constant NE rate in the MPZ with characteristic timescales of tens of minutes (Fig. 5h,i). Inhibiting myosin II activity with blebbistatin causes a reduction in the magnitude of cell–cell contact fluctuations (Fig. 5f and Methods) and a decrease of nearly 50% in the NE rate (Fig. 5i), indicating that the measured NE events in the MPZ are actively induced by actomyosin-generated tension fluctuations. While NE events in the tissue directly adjacent to the droplet display the same NE rate as the rest of the MPZ in the final stages of droplet relaxation (40–55 min; Fig. 5g–i), the NE rate close to the droplet is higher than the rest of the MPZ during the beginning of droplet relaxation (0–15 min; Fig. 5g–i). This observed initial excess of NE events close to the droplet indicates the presence of passive NE events caused by the capillary stresses imposed by the droplet on the tissue during its relaxation, as predicted theoretically (Fig. 4c). The measured low and constant rate of active NE events in the MPZ is consistent with the measured stretched-exponential behaviour of the stress relaxation at long timescales (tens of minutes), and indicates that tissue fluidization is largely caused by active NE events arising from tension fluctuations at cell–cell contacts.

To characterize the relative roles of tension fluctuations and cell–cell adhesion in rigidity transitions, we used N-cadherin ($cdh2^{-/-}$) mutants lacking N-cadherin mediated cell–cell adhesion[46] (Methods). While the MPZ tissue in wild-type embryos is fluidized by active NE events (Fig. 5d–i) and displays cellular movements and mean squared relative displacements (MSRD) compatible with cell uncaging (Fig. 5j,k), the presomitic mesoderm (PSM) has been shown to be in a solid-like state[15], with cells caged by their neighbours (MSRD ≪ 1 at 30 min; Fig. 5j,k). Our measurements indicate that cell movements in the PSM of N-cadherin ($cdh2^{-/-}$) mutants, a tissue that has been shown to be characterized by reduced cell volume fraction and lower yield stress but similar cell–cell contact fluctuations as wild-type embryos[15], display the same MSRD behaviour as wild-type embryos (Fig. 5k). These results indicate that lowering cell–cell adhesion while maintaining low cell–cell contact fluctuations does not allow cells to uncage themselves to remodel the tissue.

Altogether, both our computational and experimental results indicate that actomyosin-generated tension fluctuations actively drive structural rearrangements that cause stress relaxation in the tissue, thereby controlling tissue fluidization and enabling tissue remodelling.

Online content

Any methods, additional references, Nature Research reporting summaries, source data, extended data, supplementary information, acknowledgements, peer review information; details of author contributions and competing interests; and statements of data and code availability are available at https://doi.org/10.1038/s41567-021-01215-1.

References

1. Heisenberg, C.-P. & Bellaiche, Y. Forces in tissue morphogenesis and patterning. *Cell* **153**, 948–962 (2013).
2. Guillot, C. & Lecuit, T. Mechanics of epithelial tissue homeostasis and morphogenesis. *Science* **340**, 1185–1189 (2013).
3. Angelini, T. E. et al. Glass-like dynamics of collective cell migration. *Proc. Natl Acad. Sci. USA* **108**, 4714–4719 (2011).
4. Malinverno, C. et al. Endocytic reawakening of motility in jammed epithelia. *Nat. Mater.* **16**, 587–596 (2017).
5. Park, J.-A. et al. Unjamming and cell shape in the asthmatic airway epithelium. *Nat. Mater.* **14**, 1040–1048 (2015).
6. Palamidessi, A. et al. Unjamming overcomes kinetic and proliferation arrest in terminally differentiated cells and promotes collective motility of carcinoma. *Nat. Mater.* **18**, 1252–1263 (2019).
7. Sadati, M., Qazvini, N. T., Krishnan, R., Park, C. Y. & Fredberg, J. J. Differentiation. *Differentiation* **86**, 121–125 (2013).
8. Harris, A. R. et al. Characterizing the mechanics of cultured cell monolayers. *Proc. Natl Acad. Sci. USA* **109**, 16449–16454 (2012).
9. Prakash, V. N., Bull, M. S. & Prakash, M. Motility-induced fracture reveals a ductile-to-brittle crossover in a simple animal's epithelia. *Nat. Phys.* https://doi.org/10.1038/s41567-020-01134-7 (2021).
10. Schotz, E. M., Lanio, M., Talbot, J. A. & Manning, M. L. Glassy dynamics in three-dimensional embryonic tissues. *J. R. Soc. Interface* **10**, 20130726 (2013).
11. Petridou, N. I., Grigolon, S., Salbreux, G., Hannezo, E. & Heisenberg, C.-P. Fluidization-mediated tissue spreading by mitotic cell rounding and non-canonical Wnt signalling. *Nat. Cell Biol.* **21**, 169–178 (2019).
12. Atia, L. et al. Geometric constraints during epithelial jamming. *Nat. Phys.* **14**, 613–620 (2018).
13. Firmino, J., Rocancourt, D., Saadaoui, M., Moreau, C. & Gros, J. Cell division drives epithelial cell rearrangements during gastrulation in chick. *Dev. Cell* **36**, 249–261 (2016).
14. Ranft, J. et al. Fluidization of tissues by cell division and apoptosis. *Proc. Natl Acad. Sci. USA* **107**, 20863–20868 (2010).
15. Mongera, A. et al. A fluid-to-solid jamming transition underlies vertebrate body axis elongation. *Nature* **561**, 401–405 (2018).
16. Noll, N., Mani, M., Heemskerk, I., Streichan, S. J. & Shraiman, B. I. Active tension network model suggests an exotic mechanical state realized in epithelial tissues. *Nat. Phys.* **13**, 1221–1226 (2017).
17. Bi, D., Lopez, J. H., Schwarz, J. M. & Manning, M. L. A density-independent rigidity transition in biological tissues. *Nat. Phys.* **11**, 1074–1079 (2015).
18. Kim, S. & Hilgenfeldt, S. Cell shapes and patterns as quantitative indicators of tissue stress in the plant epidermis. *Soft Matter* **11**, 7270–7275 (2015).
19. Bi, D., Lopez, J. H., Schwarz, J. M. & Manning, M. L. Energy barriers and cell migration in densely packed tissues. *Soft Matter* **10**, 1885–1890 (2014).
20. Staple, D. et al. Mechanics and remodelling of cell packings in epithelia. *Eur. Phys. J. E* **33**, 117–127 (2010).
21. Farhadifar, R., Röper, J.-C., Aigouy, B., Eaton, S. & Jülicher, F. The influence of cell mechanics, cell–cell interactions, and proliferation on epithelial packing. *Curr. Biol.* **17**, 2095–2104 (2007).
22. Graner, Fmc & Glazier, J. A. Simulation of biological cell sorting using a two-dimensional extended Potts model. *Phys. Rev. Lett.* **69**, 2013–2016 (1992).
23. Chiang, M. & Marenduzzo, D. Glass transitions in the cellular Potts model. *Europhys. Lett.* **116**, 28009 (2016).
24. Boromand, A., Signoriello, A., Ye, F., O'Hern, C. S. & Shattuck, M. D. Jamming of deformable polygons. *Phys. Rev. Lett.* **121**, 248003 (2018).
25. Perrone, M. C., Veldhuis, J. H. & Brodland, G. W. Non-straight cell edges are important to invasion and engulfment as demonstrated by cell mechanics model. *Biomech. Model. Mechanobiol.* **15**, 405–418 (2016).
26. Graner, F. & Sawada, Y. Can surface adhesion drive cell rearrangement? Part II: a geometrical model. *J. Theor. Biol.* **164**, 477–506 (1993).
27. Teomy, E., Kessler, D. A. & Levine, H. Confluent and nonconfluent phases in a model of cell tissue. *Phys. Rev. E* **98**, 042418 (2018).
28. Boromand, A. et al. The role of deformability in determining the structural and mechanical properties of bubbles and emulsions. *Soft Matter* **15**, 5854–5865 (2019).
29. Henkes, S., Fily, Y. & Marchetti, M. C. Active jamming: self-propelled soft particles at high density. *Phys. Rev. E* **84**, 040301 (2011).
30. Bi, D., Yang, X., Marchetti, M. C. & Manning, M. L. Motility-driven glass and jamming transitions in biological tissues. *Phys. Rev. X* **6**, 021011 (2016).

31. Sumi, A. et al. Adherens junction length during tissue contraction is controlled by the mechanosensitive activity of actomyosin and junctional recycling. *Dev. Cell* **47**, 453–463.e3 (2018).

32. Curran, S. et al. Myosin II controls junction fluctuations to guide epithelial tissue ordering. *Dev. Cell* **43**, 480–492.e6 (2017).

33. Krajnc, M. Solid–fluid transition and cell sorting in epithelia with junctional tension fluctuations. *Soft Matter* **16**, 3209–3215 (2020).

34. Aveyard, R. et al. Flocculation transitions of weakly charged oil-in-water emulsions stabilized by different surfactants. *Langmuir* **18**, 3487–3494 (2002).

35. Trappe, V., Prasad, V., Cipelletti, L., Segre, P. N. & Weitz, D. A. Jamming phase diagram for attractive particles. *Nature* **411**, 772–775 (2001).

36. O'Hern, C. S., Silbert, L. E., Liu, A. J. & Nagel, S. R. Jamming at zero temperature and zero applied stress: the epitome of disorder. *Phys. Rev. E* **68**, 011306 (2003).

37. Wang, X. et al. Anisotropy links cell shapes to tissue flow during convergent extension. *Proc. Natl Acad. Sci. USA* **117**, 13541–13551 (2020).

38. Kim, S., Wang, Y. & Hilgenfeldt, S. Universal features of metastable state energies in cellular matter. *Phys. Rev. Lett.* **120**, 248001 (2018).

39. Bonn, D., Denn, M. M., Berthier, L., Divoux, T. & Manneville, S. Yield stress materials in soft condensed matter. *Rev. Mod. Phys.* **89**, 035005 (2017).

40. Abou, B., Bonn, D. & Meunier, J. Aging dynamics in a colloidal glass. *Phys. Rev. E* **64**, 243–246 (2001).

41. Phillips, J. C. Stretched exponential relaxation in molecular and electronic glasses. *Rep. Prog. Phys.* **59**, 1133–1207 (1996).

42. Bambardekar, K., Clément, R., Blanc, O., Chardès, C. & Lenne, P.-F. Direct laser manipulation reveals the mechanics of cell contacts in vivo. *Proc. Natl Acad. Sci. USA* **112**, 1416–1421 (2015).

43. Serwane, F. et al. In vivo quantification of spatially varying mechanical properties in developing tissues. *Nat. Methods* **14**, 181–186 (2017).

44. Lawton, A. K. et al. Regulated tissue fluidity steers zebrafish body elongation. *Development* **140**, 573–582 (2013).

45. Banavar, S. P. et al. Mechanical control of tissue shape and morphogenetic flows during vertebrate body axis elongation. Preprint at *bioRxiv* https://doi.org/10.1101/2020.06.17.157586 (2020).

46. Lele, Z. et al. *parachute/n-cadherin* is required for morphogenesis and maintained integrity of the zebrafish neural tube. *Development* **129**, 3281–3294 (2002).

Methods

Pressure and volume relation. The (osmotic) pressure P of a cell has been experimentally shown to vary with its volume according to $P = K/V$ (ref. [47]), meaning that changes in the osmotic pressure difference between the inside (P) and outside (P_0) of the cell lead to changes in the cell volume V, with K characterizing the cell compressibility (we assumed for simplicity that cells are never compressed close to their dry mass limit). In our 2D description, the cell area A plays the role of the volume, so that $P = K/A$, with the characteristic cell size L_0 (or preferred area $A_0 = L_0^2$) being set by this relation, namely $L_0 \equiv \sqrt{K/P_0}$. However, while we use the experimentally measured relation between osmotic pressure and cell volume[47] (area in 2D), the specific P–V (or P–A) functional form does not change our results qualitatively as long as the cell volume decreases with increasing applied osmotic pressure, namely $P - P_0 = -\Gamma(A - A_0)$ (with Γ being a coefficient characterizing the cell's compressibility), and the deviations from the preferred cell area in 2D (A_0) are mild.

Fixed point tension and tension dynamics. The fixed point tension, T_{ij}^0, corresponds to an average effective tension at cell–cell contacts and has contributions from the average actomyosin-generated cortical tension T_0 in each cell and the average cell–cell adhesion strength W, so that $T_{ij}^0 = 2T_0 - W$ (Fig. 1b). At free cell boundaries (cell boundaries contacting the extracellular space), the average effective tension is just the average cortical tension of the cell, namely $T_{ij}^0 = T_0$. Here we assume the average tension T_0 not to change with the cell perimeter, as no current experimental observations suggest that dependence. In situations where the cell shape becomes very anisotropic or contorted enough to have very large perimeters, a dependence of the average effective tension on the perimeter could potentially arise from limitations in plasma membrane availability.

The stochastic dynamics of tensions depends on the magnitude of tension fluctuations, which is ΔT at cell–cell contacts and $\Delta T/2$ at free cell boundaries (cell boundaries contacting the extracellular space).

Parameter estimation. Since the relaxation timescale τ_R has been measured to be much smaller than the persistence timescale of tension variations ($\tau_R \lesssim 20\,\mathrm{s}$ (refs. [42,43]); $\tau_T \simeq 90\,\mathrm{s}$ (ref. [15])), we set the ratio to $\tau_T/\tau_R = 10$. While the values of osmotic pressure are unknown in vivo, they are expected to be larger than cortical stresses[47], so that $P_0L_0/T_0 \gg 1$. Consequently, we fix $P_0L_0/T_0 = 10$ for all simulations. This ensures relatively mild cell size variations, as observed experimentally[15]. Fixing these parameters reduces the parameter space to the normalized amplitude of tension fluctuations $\Delta T/T_0$, the ratio W/T_0 of average adhesion strength and average cortical tension, and the ratio NL_0^2/A_T of the cell's total preferred area and the total available area.

Numerical integration. The dimensionless version of the governing equations (equations (1) and (2)) was integrated numerically using the Euler–Maruyama method with a time step, Δt. We used $\Delta t = 0.005\tau_R$ for all simulations to have a time resolution much smaller than the smallest characteristic timescale in the system, τ_R.

Initial configuration generation protocol. A polygonal tiling of confluent states is first generated by random Poisson Voronoi tessellation in a square periodic box of total area A_T. Before the introduction of extracellular spaces, the initial confluent configuration is first annealed to a local equilibrium state to prevent sudden adjustment of cell shape with extracellular spaces. Extracellular spaces are introduced by replacing each vertex in the confluent configurations with a small triangular extracellular space 'cell' centred around the original vertex position, and with the three new vertices located on the each of the original edges and of 1% their original length. Small tension fluctuations ($\Delta T/T_0 = 0.5$) are applied for a duration τ_T. The resulting configuration is used as an initial configuration for simulations of both equilibrium configurations and dynamics.

As for any model of multicellular systems, some of the observed configurations depend on the initialization protocol. Regular hexagonal packings can be obtained by choosing regularly arranged initial cellular configurations. However, since most embryonic tissues typically show topologically disordered configurations, we used random Poisson Voronoi tessellation as an initial configuration.

Equilibrium configurations and quasi-static changes. Equilibrium states were obtained by quenching the system from an initial state with tension fluctuations ($\Delta T/T_0 = 0.5$) to an equilibrium state ($\Delta T/T_0 = 0$) for each parameter set. While we observe small changes in the resulting configurations if the magnitude of the initial tension fluctuations is varied in the annealing protocol, our results, including the existence of the structural transition, remain qualitatively unchanged. Quasi-static changes of the relative adhesion at equilibrium where performed by first quenching the system to equilibrium at a given parameter value, and then performing a small change in the parameter (W/T_0) and letting the system relax. Specifically, the system was initialized at a large value of the relative adhesion strength that ensured a confluent state ($W/T_0 = 1$) and then quenched to a local equilibrium state. The relative adhesion strength was then progressively reduced to $W/T_0 = 0$ by small

changes ($\Delta W/T_0 = -0.02$). Similarly, the other branch was found by initializing the system at zero adhesion strength ($W/T_0 = 0$) and progressively increasing it to $W/T_0 = 1$ by small increments ($\Delta W/T_0 = 0.02$). After each adhesion adjustment, the system is relaxed to local equilibrium states.

Introducing spaces between cells. Extracellular spaces are first introduced to initial configurations of confluent states as cells with different properties. Each vertex is replaced by a small triangular extracellular space centred around the original vertex position, and with the three new vertices located on the each of the original edges and of 1% their original length. These extracellular spaces then behave like 'cells' with different properties (see above) and their size and geometrical features are determined by force balance at the vertices, as is the case for cells too. When two extracellular space 'cells' become neighbours, they are merged. This implementation allows non-confluent states in vertex models and is different from previous descriptions of non-confluent states, which used centre particles[26,27] or deformable particles models[28].

Intermediate non-physical vertices. Intermediate vertices are introduced for both cell–cell contacts and free cell boundaries to allow for more realistic cell shapes. With intermediate vertices, individual edges consist of linear segments joined together to form a piecewise linear edge. The desired segment length is introduced as a parameter and the number of intermediate vertices for each edge is equal to the closest lower integer given by the ratio of instantaneous edge length to the segment length criterion. When the edge length increases (decreases), an intermediate vertex can be added (deleted) following the criterion just described. As the number of intermediate vertices changes, intermediate vertex positions are reassigned uniformly along the edge. If the longest segment is longer than twice the shortest segment in a given edge, intermediate vertex positions are also reassigned uniformly along the piecewise linear line. This implementation of intermediate vertices is similar to the one used for confluent equilibrium systems[25].

While we considered all vertices to have the same drag coefficient, physical and non-physical vertices may, in general, be characterized by different drag coefficients. This approximation is not due to technical reasons, as the simulation framework presented here can simulate different drag coefficients at different vertices different drag coefficients. Previous studies have shown that the measured stress relaxation timescales for movement of vertices is much smaller (~1–20 s (refs. [42,43])) than the persistence timescale of active tension fluctuations, which is approximately 100 s (ref. [15]). Since we are interested in the behaviour of the system at long timescales (longer than the persistence timescale of active tension fluctuations ($t \gg \tau_T$)) and the timescales associated with viscous relaxation at vertices are much smaller than the persistence timescale of active stresses ($\tau_T \gg \tau_R$), we neglected the differences in drag coefficient at the different vertices, as they are irrelevant in this limit.

Treatment of topological transitions. T1 transitions occurs in our description when a given edge length is shorter than a critical length $\ell_c = 0.01 \times 2\pi L_0$. When a T1 transition leads to the formation of a new vertex between three cells, we introduce a small triangular extracellular space 'cell' and let it evolve in time, as described above. Free cell boundaries (a boundary of a cell and the extracellular space) occasionally intersect each other due to the system dynamics. This event corresponds to the formation of a new contact between two cells. Therefore, when an intersection between any two free boundary edges is detected, a new cell–cell contact is introduced, splitting the extracellular space in two.

While not simulated here, cell divisions and cell death, which would also introduce topological transitions, are straightforward to simulate in this framework. Since these events would also induce cell rearrangements, they are also likely to enable tissue fluidization, as previously suggested[5,11,13,14].

Cell trajectories and MSD. To obtain the MSD, we first computed the cell centres (centroid of polygon), $\mathbf{r}_{C,i}$, for each time point, t, based on vertex positions. Then, the cell trajectories were obtained by monitoring the changes of cell centres. Using the cell trajectories $\mathbf{r}_{C,i}(t)$, we obtained the MSD according to

$$\mathrm{MSD}(t) = \frac{1}{N} \sum_i \left(\mathbf{r}_{C,i}(t_0 + t) - \mathbf{r}_{C,i}(t) \right)^2 . \tag{3}$$

MSD values were averaged over all cells and also all initial timepoints t_0 for any given set of model parameters.

Application of a step strain. Since tissue fluidization in biological tissues is associated with their nonlinear mechanical response[15], we impose large strains ϵ_{xy} of 150%. The large step strain was applied by deforming the simulation box from a square to a parallelogram of the target shear strain, namely 150%. An affine deformation is applied to all vertex positions when imposing the step strain. Lees–Edwards periodic boundary conditions were imposed throughout the simulation to avoid mismatch of cell geometry across system boundaries.

Stress calculation. The non-dimensional stress tensor can be computed from the transient tissue geometry with knowledge of junctional tensions and cell pressures[48,49] (lowercase indicates normalized quantities), namely

$$\sigma_{mn} = \rho \left[-\sum_{i:\text{cell}} \Delta p_i a_i \delta_{mn} + \sum_{ij:\text{edge}} t_{ij} \frac{l_{ij,m}\, l_{ij,n}}{|\mathbf{l}_{ij}|} \right], \quad (4)$$

where $\Delta p_i \equiv p_i - p_0$, m and n are indices indicating the spatial direction ($m = x, y$ and $n = x, y$), a_i is the dimensionless cell area, $\mathbf{l}_{ij}$ is the vector form of the edge length between cells i and j, and δ_{mn} is the Kronecker delta. The shear-stress term can be written as

$$\sigma_{xy} = \rho \left[\sum_{ij:\text{edge}} t_{ij} \frac{l_{ij,x}\, l_{ij,y}}{|\mathbf{l}_{ij}|} \right]. \quad (5)$$

Active shear stress. Due to tension fluctuations, the macroscopic shear stress shows fluctuations around zero. To quantify the magnitude of these active shear-stress fluctuations, the shear-stress values are monitored over a time interval of $10\tau_R$ and their standard deviation is computed for each parameter set (no macroscopic imposed strain). The level of active shear stress corresponds to the computed standard deviation of shear stress, and increases approximately linearly with the magnitude of tension fluctuations for a given relative cell adhesion strength (Supplementary Section 2).

Zebrafish husbandry, lines and experimental manipulations. Zebrafish (*Danio rerio*) were maintained under standard conditions[50]. The cdh2[tm101] mutant line[46] was used to disrupt adhesions between cells, otherwise phenotypically wild-type lines were used. Animal husbandry and experiments were done according to protocols approved by the Institutional Animal Care and Use Committee (IACUC) at the University of California Santa Barbara. Transgenic lines Tg(hsp70:secP-mCherry)[p1] (ref. [51]) and Tg(h2afva:eGFP)[kca6] were used to visualize extracellular spaces and nuclei, respectively. Both Tg(bact2:mem-neonGreen-neonGreen)[hm40] and Tg(actb2:memCherry2)[hm29] transgenic lines were used to visualize cell membranes in different experiments. In some cases, membranes were labelled by injection with 80–100 pg membrane-GFP messenger RNA at the 1-2 cell stage.

Imaging. In all cases, 8–10 somite stage zebrafish embryos were mounted in 1% low-melting point agarose in a glass bottom Petri dish (MatTek Corporation) for a dorsal view of the tailbud and imaged at 25 °C using a ×40 water immersion objective (LD C-Apochromat 1.1 W, Carl Zeiss) on an inverted Zeiss Laser Scanning Confocal (LSM 710, Carl Zeiss).

For kymograph of cell–cell contacts, confocal timelapse data of the MPZ and the PSM regions in Tg(h2afva:eGFP)[kca6] × Tg(actb2:memCherry2)[hm29] double transgenic embryos were acquired (2 s time intervals for 30 min). The intensity profile of a single junction was tracked over 300 s and measured over a 5-pixel-width segment line to minimize the error induced by the estimation of the junction location.

Images of extracellular spaces were obtained using an outcross of Tg(hsp70:secP-mCherry)[p1] (refs. [51]) and Tg(bact2:mem-neonGreen-neonGreen)[hm40], to label the extracellular spaces and cell membranes, respectively. To trigger the expression of mCherry in the extracellular space, a 1 h heat shock in a water bath at 39 °C was performed when the embryos were at 75% epiboly stage. Confocal sections through the PSM and the MPZ tissues were subsequently acquired.

Imaging of ferrofluid droplets was done as previously reported[15,43]. Briefly, images of a droplet previously inserted in the MPZ region of the embryo were taken every 5 s. Ferrofluid droplets were fluorescently labelled using a custom-synthesized fluorous cyanine dye FCy5 dissolved in the fluorocarbon-based ferrofluid oil at a final concentration of 25 μM (ref. [52]).

Tracking of cell movements in the PSM of N-cadherin mutants. Both mutant ($cdh2^{-/-}$) and sibling ($cdh2^{+/+;+/-}$) embryos were injected with 80–100 pg each of H2B-mRFP mRNA and membrane-GFP mRNA at the 1-2 cell stage to label nuclei and membranes, respectively. Confocal stacks through the PSM were acquired with a z-step size of 1 μm and time interval of 1 min for 30 min, and processed using Imaris (Bitplane). Data were smoothed using a 1 pixel Gaussian filter, to correct for photobleaching over time the normalize timepoints function was used, then attenuation correction was applied to correct for z attenuation. After processing, data were cropped to the tissue of interest, then nuclei were detected using the spots function, and tracked using the Brownian motion algorithm. Nuclei positions were output for further analyses. The MSRD is calculated from the cell trajectories and normalized using the cell diameter d. The normalized MSRD is MSRD/d^2 (ref. [15]).

Generation and injection of ferrofluid droplets. Ferrofluid droplets were prepared as previously described[15,43]. Briefly, DFF1 ferrofluid (Ferrotec) was diluted in filtered 3M Novec 7300 fluorocarbon oil. To prevent non-specific adhesion between cells and droplets, a fluorinated Krytox-PEG(600) surfactant (008-fluorosurfactant, RAN Biotechnologies[53]) was diluted in the ferrofluid at a 2.5% (w/w) concentration. The ferrofluid was calibrated before each experiment as previously described[43], so that the applied magnetic stresses are known. Once prepared and calibrated, the ferrofluid was injected in the MPZ tissue of phenotypically wild-type zebrafish embryos at the 4-6 somite stage to form droplets of 30–40 μm diameter, as previously described[15,43]. Imaging of droplets started at least 1.5 h after the injection to let the tissue fully recover from it.

Magnetic actuation of ferrofluid microdroplets. Actuation of ferrofluid droplets was performed following the previously described protocol[43]. Briefly, ferrofluid droplets were actuated by a uniform and constant magnetic field[43] applied along the direction of smaller droplet deformation, as given by the smallest semi-axis of elliptical deformation before the magnetic field was applied. The droplet shape was monitored before (15 min) and during magnetic actuation (15 min), as well as during droplet relaxation (1 h).

Measurements of strain and stress relaxation. On application of a uniform, constant magnetic field, ferrofluid droplets acquire an ellipsoidal shape, elongated along the direction of the applied magnetic field and symmetrical about it[43,54]. The observed confocal section through the middle of the droplet was fitted to an ellipse of short and long semi-axes a and b, respectively, as previously described[43]. The droplet strain, $(b - b_0)/R$, is defined as the ratio of its elongation along the direction of applied magnetic field, namely $(b - b_0)$ (with b_0 being the value of b just before magnetic actuation), and the droplet radius R, and can be monitored over time by measuring the change in the droplet long semi-axis $b(t)$. The stresses at supracellular (tissue) scales associated with a particular droplet deformation were obtained from the elliptical droplet deformation, as previously described[15], namely $\sigma_A = 2\gamma (H_b - H_a)$, where γ is the droplet interfacial tension and H_b and H_a are the mean curvatures of the droplet ellipsoidal shape at the intersection of the principal axis with the fitted ellipsoid. Since the droplet shape is that of a prolate spheroid, H_b and H_a read $H_b = b/a^2$ and $H_a = 1/2a + a/(2b^2)$. By monitoring the changes in droplet shape over time, we obtained the time evolution of both the mean curvatures, namely $H_b(t)$ and $H_a(t)$. The droplet interfacial tension γ was measured in each experiment in situ and in vivo, as previously described[15,43]. Using the measured value of the interfacial tension for each droplet and the time evolution of the mean curvatures $H_b(t)$ and $H_a(t)$, we obtained the time evolution of the stresses during relaxation using $\sigma_A(t) = 2\gamma (H_b(t) - H_a(t))$.

NE analysis. One-hour-long confocal timelapses of the MPZ region of membrane-labelled embryos containing a previously inserted droplet were acquired at 1 frame every 5 s. A region of the MPZ away from the droplet and a region adjacent to the droplet were cropped and the time at which T1 transitions occurred in each region was recorded. T1 transitions were detected manually by inspecting cell configurations between frames. To improve the accuracy of the analysis, smaller sections of each region containing approximately 10 to 15 cells were further cropped and analysed separately. The cumulative NE were obtained by adding up the NE events occurring over time in each region. The NE rate was obtained by taking the derivative of the cumulative NE function.

Reporting Summary. Further information on research design is available in the Nature Research Reporting Summary linked to this article.

Data availability
Source data are provided with this paper.

Code availability
The code developed for this paper is available in Supplementary Software 1.

References
47. Guo, M. et al. Cell volume change through water efflux impacts cell stiffness and stem cell fate. *Proc. Natl Acad. Sci. USA* **114**, E8618–E8627 (2017).
48. Ishihara, S. & Sugimura, K. Bayesian inference of force dynamics during morphogenesis. *J. Theor. Biol.* **313**, 201–211 (2012).
49. Yang, X. et al. Correlating cell shape and cellular stress in motile confluent tissues. *Proc. Natl Acad. Sci. USA* **114**, 12663–12668 (2017).
50. Nüsslein-Volhard, C. & Dahm, R. *Zebrafish: A Practical Approach* (Oxford Univ. Press, 2002).
51. Wang, J. et al. Anosmin1 shuttles Fgf to facilitate its diffusion, increase its local concentration, and induce sensory organs. *Dev. Cell* **46**, 751–766.e12 (2018).
52. Lim, I. et al. Fluorous soluble cyanine dyes for visualizing perfluorocarbons in living systems. *J. Am. Chem. Soc.* **142**, 16072–16081 (2020).

53. Holtze, C. et al. Biocompatible surfactants for water-in-fluorocarbon emulsions. *Lab Chip* **8**, 1632–1639 (2008).
54. Rowghanian, P., Meinhart, C. D. & Campas, O. Dynamics of ferrofluid drop deformations under spatially uniform magnetic fields. *J. Fluid Mech.* **802**, 245–262 (2016).

Author contributions

S.K. and O.C. designed research; S.K. implemented and performed the simulations; M.P. and G.A.S.-V. performed experiments; S.K., M.P. and G.A.S.-V. analysed data; S.K. and O.C. wrote the paper; O.C. supervised the project.

Competing interests

The authors declare no competing interests.

Additional information

Extended data is available for this paper at https://doi.org/10.1038/s41567-021-01215-1.

Supplementary information The online version contains supplementary material available at https://doi.org/10.1038/s41567-021-01215-1.

**Correspondence and requests for materials** should be addressed to O.C.

Peer review information *Nature Physics* thanks the anonymous reviewers for their contribution to the peer review of this work.

Reprints and permissions information is available at www.nature.com/reprints.
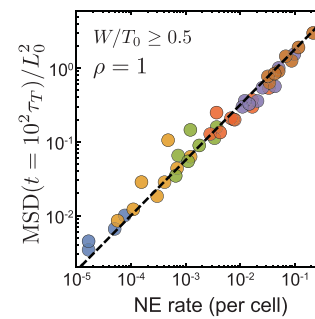
Extended Data Fig. 1 | Power law relation between NE rate and MSD at long timescales. Power law relation between long time MSD values and NE rate when the systems are close to confluence for high adhesion levels. NE rate and longtime MSD show a power law relation with an exponent of 0.75.
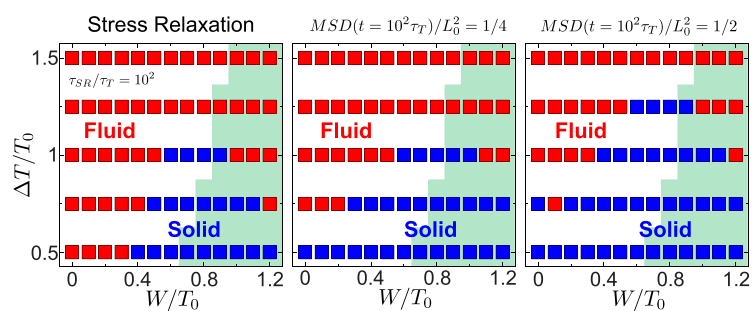
Extended Data Fig. 2 | Comparison of solid/fluid phase diagrams obtained from stress relaxation and from cell movements. Solid/fluid phase diagrams determined by mechanical measurement of stress relaxation (left) and cell movements, MSD=1/2 (middle) and MSD=1/4 (right). Green region indicates confluent states.

nature research

Corresponding author(s):   Otger Campas

Last updated by author(s):   Feb 15, 2021

Reporting Summary

Nature Research wishes to improve the reproducibility of the work that we publish. This form provides structure for consistency and transparency in reporting. For further information on Nature Research policies, see our Editorial Policies and the Editorial Policy Checklist.

Statistics

For all statistical analyses, confirm that the following items are present in the figure legend, table legend, main text, or Methods section.

n/a	Confirmed	
☐	☒	The exact sample size (*n*) for each experimental group/condition, given as a discrete number and unit of measurement
☐	☒	A statement on whether measurements were taken from distinct samples or whether the same sample was measured repeatedly
☒	☐	The statistical test(s) used AND whether they are one- or two-sided *Only common tests should be described solely by name; describe more complex techniques in the Methods section.*
☒	☐	A description of all covariates tested
☒	☐	A description of any assumptions or corrections, such as tests of normality and adjustment for multiple comparisons
☒	☐	A full description of the statistical parameters including central tendency (e.g. means) or other basic estimates (e.g. regression coefficient) AND variation (e.g. standard deviation) or associated estimates of uncertainty (e.g. confidence intervals)
☒	☐	For null hypothesis testing, the test statistic (e.g. *F*, *t*, *r*) with confidence intervals, effect sizes, degrees of freedom and *P* value noted *Give P values as exact values whenever suitable.*
☒	☐	For Bayesian analysis, information on the choice of priors and Markov chain Monte Carlo settings
☒	☐	For hierarchical and complex designs, identification of the appropriate level for tests and full reporting of outcomes
☒	☐	Estimates of effect sizes (e.g. Cohen's *d*, Pearson's *r*), indicating how they were calculated

Our web collection on statistics for biologists contains articles on many of the points above.

Software and code

Policy information about availability of computer code

Data collection	Commercial Zeiss Zen software was used to perform confocal imaging. Computer simulations were done in Matlab 9.6 (MathWorks).
Data analysis	Commercial software used to analyze data: Imaris 9.3 (Bitplane) and Matlab 9.6 (MathWorks). ImageJ was also used to analyze data.

For manuscripts utilizing custom algorithms or software that are central to the research but not yet described in published literature, software must be made available to editors and reviewers. We strongly encourage code deposition in a community repository (e.g. GitHub). See the Nature Research guidelines for submitting code & software for further information.

Data

Policy information about availability of data

All manuscripts must include a data availability statement. This statement should provide the following information, where applicable:

- Accession codes, unique identifiers, or web links for publicly available datasets
- A list of figures that have associated raw data
- A description of any restrictions on data availability

Source data supporting these findings are available online as Supplementary Data.

Field-specific reporting

Please select the one below that is the best fit for your research. If you are not sure, read the appropriate sections before making your selection.

☒ Life sciences ☐ Behavioural & social sciences ☐ Ecological, evolutionary & environmental sciences

For a reference copy of the document with all sections, see nature.com/documents/nr-reporting-summary-flat.pdf

Life sciences study design

All studies must disclose on these points even when the disclosure is negative.

Sample size	Sample size was chosen so that statistical variation of the data did not change considerably upon addition of more data points.
Data exclusions	No data was excluded.
Replication	Independent experiments were performed and statistical analysis done independently of these data sets. The results obtained were the same within error bars in different, independent data sets.
Randomization	No specific experimental groups were defined and all data was considered.
Blinding	Analysis was done by automated software which was blind to data collection.

Reporting for specific materials, systems and methods

We require information from authors about some types of materials, experimental systems and methods used in many studies. Here, indicate whether each material, system or method listed is relevant to your study. If you are not sure if a list item applies to your research, read the appropriate section before selecting a response.

Materials & experimental systems

n/a	Involved in the study
☒	Antibodies
☒	Eukaryotic cell lines
☒	Palaeontology and archaeology
☐	☒ Animals and other organisms
☒	Human research participants
☒	Clinical data
☒	Dual use research of concern

Methods

n/a	Involved in the study
☒	ChIP-seq
☒	Flow cytometry
☒	MRI-based neuroimaging

Animals and other organisms

Policy information about studies involving animals; ARRIVE guidelines recommended for reporting animal research

Laboratory animals	Zebrafish (Danio rerio) were used in this study. Since only embryos were studied, sex-specific experiments were not necessary, as zebrafish embryos at the studies stage have not yet undergone sex determination.
Wild animals	None.
Field-collected samples	None.
Ethics oversight	Animal husbandry and experiments were done according to protocols approved by the Institutional Animal Care and Use Committee (IACUC) at the University of California Santa Barbara.

Note that full information on the approval of the study protocol must also be provided in the manuscript.